Chemical Science

ROYAL SOCIETY OF CHEMISTRY

EDGE ARTICLE

View Article Online
View Journal | View Issue

Cite this: *Chem. Sci.*, 2024, **15**, 11528

All publication charges for this article have been paid for by the Royal Society of Chemistry

A "dual-key-and-lock" DNA nanodevice enables spatially controlled multimodal imaging and combined cancer therapy†

Shuzhen Yue, [a] Jiayin Zhan,[a] Xuan Xu,[a] Junpeng Xu,*[c] Sai Bi *[b]
and Jun-Jie Zhu *[a]

Received 4th March 2024
Accepted 15th June 2024

DOI: 10.1039/d4sc01493f

rsc.li/chemical-science

DNA-based theragnostic platforms have attracted more and more attention, while their applications are still impeded by nonspecific interference and insufficient therapeutic efficacy. Herein, we fabricate an integrated "dual-key-and-lock" DNA nanodevice (DKL-DND) which is composed of the inner Dox/Hairpin/Aptazyme-Au@Ag@Au probes and the outer metal–organic frameworks loaded with Fuel strand. Once internalized into human breast cancer cells (MCF-7), the DKL-DND is activated by cascaded endogenous stimuli (acidic pH in the lysosome and high expression of ATP in the cytoplasm), leading to spatially controlled optical/magnetic resonance multimodal imaging and gene/chemo/small molecule combined cancer therapy. By engineering pH and ATP-responsive units as cascaded locks on the DKL-DND, the operating status of the nanodevice and accessibility of encapsulated anti-tumour drugs can be precisely regulated in the specified physiological states, avoiding the premature activation and release during assembly and delivery. Both *in vitro* and *in vivo* assessments demonstrate that the DKL-DND with excellent stimuli-responsive ability, biocompatibility, stability and accumulation behaviour was capable of simultaneously affording accurate tumour diagnosis and efficient tumour growth inhibition. This integrated DKL-DND exhibits great promise in constructing self-adaptive nanodevices for multimodal imaging-guided combination therapy.

Introduction

During the past few decades, plenty of bottom-up biomimetic methodologies have been reported to construct a variety of dynamic structures *via* assembly of synthetic moieties to fulfil complex tasks.[1,2] Governed by the Watson–Crick base paring rules, DNAs with unique programmability and affordability have become unparalleled scaffolds for engineering nanodevices and molecular machines.[3,4] In particular, owing to the easy-to-predict thermodynamics and good biocompatibility, such DNA-based nanostructures have exhibited excellent performance when interacting with biological elements, which show great promise in biosensing and bioimaging,[5,6] specific cargo delivery,[7,8] molecule computation,[9–11] and so on. Despite the progress made, the majority of current DNA nanodevices still operate in an "always on" model. In fact, certain biomarkers overexpressed in tumour cells are widely distributed in solid tumour microenvironment and systemic circulation.[12–15] Thus, the "always on" DNA nanodevices lacking spatiotemporal selectivity could inevitably interact with the undesired targets during the delivery process, resulting in nonspecific activation and false-positive signals.

Recently, some "on-demand" activated DNA nanodevices have been developed for monitoring desired biomolecules.[16] In particular, the endogenous stimuli-controlled strategies (*e.g.* pH,[17] small molecules,[18] enzymes,[19,20] *etc.*) have become prominent tools for regulating the specific imaging ability of DNA nanodevices, in which the use of endogenous substances can maintain the native state of live entities and avoid organ injuries. However, most of these devices are single-locked designs, which still exist the problem of off-tumour activation due to the complex biological environments and would largely compromise the tumour-specific detection. Therefore, creating DNA nanodevices with excellent spatial controllability still remains critical to develop precise medical platforms for molecular diagnosis.

---

[a] *State Key Laboratory of Analytical Chemistry for Life Science, School of Chemistry and Chemical Engineering, Nanjing University, Nanjing 210023, P. R. China. E-mail: jjzhu@nju.edu.cn*

[b] *College of Chemistry and Chemical Engineering, Key Laboratory of Shandong Provincial Universities for Functional Molecules and Materials, Qingdao University, Qingdao 266071, P. R. China. E-mail: bisai11@126.com*

[c] *State Key Laboratory of Pharmaceutical Biotechnology, Department of Sports Medicine and Adult Reconstructive Surgery, Nanjing Drum Tower Hospital, The Affiliated Hospital of Nanjing University Medical School, Medical School, Nanjing University, Nanjing 210093, P. R. China. E-mail: xjp@nju.edu.cn*

† Electronic supplementary information (ESI) available: Additional experimental procedures and supplementary results and discussion that further support conclusions made in the main document. See DOI: **https://doi.org/10.1039/d4sc01493f**

MicroRNAs play an important role in diverse biological processes. It has been found that the aberrant expression of some specific microRNAs is closely related to the occurrence and progression of cancers.[21] Thus, the reliable analysis of microRNAs could provide valuable information for clinical diagnosis and biological study. At present, fluorescence (FL) imaging is a powerful technology for monitoring the expression and distribution of microRNA in living cells with high selectivity and spatiotemporal resolution.[22,23] However, due to the target concentration being usually extremely low and the presence of complicated biological matrices in abundance, highly sensitive *in situ* FL imaging of microRNA is still challenging. Compared with FL, surface-enhanced Raman scattering (SERS) possesses advantages including high sensitivity, "fingerprint" signatures and resistance to photobleaching, which extends our toolbox for biological analysis.[24,25] However, the nonspecific accumulation caused by low imaging speed also limits the further application of the SERS technique at the cell level.[26] Alternatively, the combination of multiple imaging modes could achieve complementary advantages of different single modes to acquire faster positioning, more accurate detection and multiscale diagnostic information.

In addition, immediate diagnosis-guided therapy can efficiently improve the survival rate of cancer patients.[27] In recent years, functional nucleic acid-assisted therapeutic platforms have shown significant potential against tumors.[28,29] For example, DNAzyme has emerged as an effective tool for gene silencing due to its advantages of flexible design and high specificity, which can catalyse the specific cleavage of intracellular mRNA to regulate the expression level of tumour-related proteins.[30] However, since tumour cells can easily bypass apoptosis through a variety of antiapoptotic signal transductions, a single-mode therapy pathway usually constrains the treatment performance. Thus, the development of combined therapy strategies integrated with precise imaging is highly demanded in biomedical research.

Motivated by the above-mentioned issues, a multifunctional DKL-DND in response to cascaded endogenous stimuli (acidic pH in the lysosome and high expression of ATP in the cytoplasm) is devised for multimodal imaging in a spatio-gated manner, accompanied by the controllable drug release for combined therapy of breast cancer. Through engineering with two customizable locks, the operation of this nanodevice can be finely manipulated by characteristic triggers, achieving on-demand activation and accurate tumour diagnosis and treatment. The fabricated DKL-DND provides a custom-made platform for spatially controllable activation *via* defining various locks in response to disease-related biomolecules, making it has considerable potential for personalized theragnostic systems based on diverse circumstances.

Results and discussion

Working principle of DKL-DND

Herein, microRNA-21 (miR-21) is selected as the model target because it is a valuable diagnostic biomarker that is commonly overexpressed in many human cancers (*e.g.* breast cancer, lung cancer, and prostate cancer).[31,32] In this system, Au@Ag@Au Double-Shell Nanoparticles (DSNPs) are first synthesized as the carrier of DNA probes, which not only exhibit excellent optical properties to enhance the SERS signal and quench FL, but also efficiently avoid the oxidation of silver by the outer gold shell to allow a good biocompatibility. The Hairpin/Aptazyme (HA) hybrids are then assembled on Au@Ag@Au DSNPs *via* Au–S covalent bonds (abbreviated as HA-DSNPs), and the anticancer drug Dox is further intercalated into the C–G region of HA hybrids (abbreviated as Dox/HA-DSNPs). Notably, to improve the spatiotemporally precise imaging ability of microRNA, the Hairpin contains a reconfigurable molecular switch to connect the miR-21 binding domains (toehold domain and branch migration domain) together, and the Aptazyme as the ATP-responsive lock is composed of the Mn^{2+}-dependent EGR-1 DNAzyme subunits (split DNAzyme 1 and split DNAzyme 2) separated by the ATP aptamer sequence. The detailed information of oligonucleotides is listed in Table S1.† Thereafter, a MOF shell as the pH-responsive lock is coated on Dox/HA-DSNPs *via* the coordination between Mn^{2+} and tannic acid (TA), followed by loading the Fuel strand (a catalytic DNA strand for signal amplification), achieving the fabrication of DKL-DND (Scheme 1A).

When the DKL-DND is internalized into MCF-7 cells *via* endocytosis (Scheme 1B), the acidic pH in the lysosome environment (pH 4.5–5.5) (Key I) promotes the rapid degradation of the MOF shell, resulting in the release of payloads including the outer Mn^{2+}, TA and Fuel strand as well as the inner Dox/HA-DSNPs. After these substrates escape from the lysosome *via* the "proton-sponge effect",[33] ATP in the cytoplasm (Key II) further induces the disassembly of HA hybrids *via* specific recognition of ATP by its aptamer domains, leading to the unlocking of DNA nanodevices for miR-21 detection. In brief, the aptamer specifically binds with ATP to form the ATP/Aptazyme complex, releasing Hairpin-DSNPs and stabilizing the catalytic loop of two splitting DNAzyme sequences. As a result, a spontaneously conformational change of molecular switch in Hairpin occurs, which thus brings the miR-21 binding domains (toehold domain and branch migration domain) in close proximity. Then, the intracellular miR-21 triggers the catalysed hairpin assembly (CHA) reaction between Hairpin and Fuel strand, forming multiple Hairpin/Fuel (HF) hybrids on Au@Ag@Au DSNPs (HF-DSNPs). In this case, the FL signal from Cy5 is quenched resulting from the distance change between Au@Ag@Au DSNPs and Cy5-tagged Fuel strand, while its SERS signal is enhanced, thus achieving FL/SERS dual-mode imaging to provide accurate expression and distribution information of miR-21 in living MCF-7 cells. Additionally, using Mn^{2+} as a T1-weighted contrast agent, magnetic resonance imaging (MRI) is carried out to obtain the multiscale tumour-related information. Moreover, the disassembly of HA hybrids results in the release of Dox and Aptazyme for chemotherapy and Mn^{2+}-mediated gene silencing on human early growth response-1 (EGR-1) mRNA, respectively. In particular, the down-regulated expression of EGR-1 can promote the curative effect of chemotherapy. Furthermore, the presence of TA enhances the therapeutic effect *via* preventing the invasion and migration of

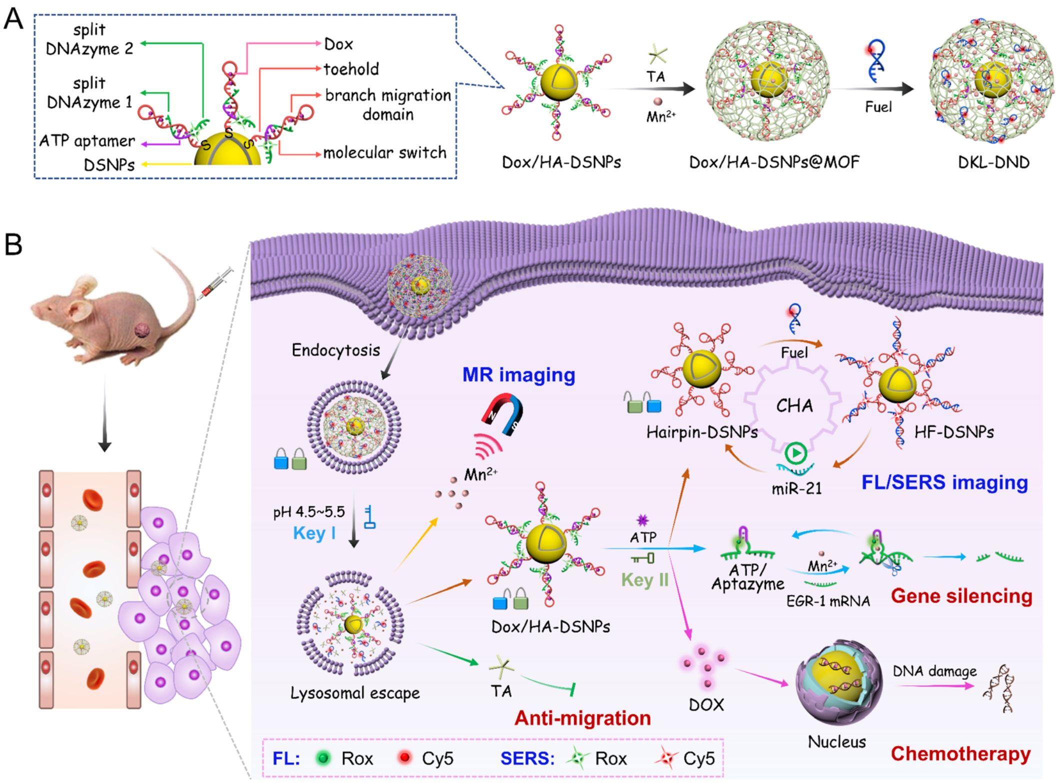

Scheme 1 Schematic illustration of the dual-key-and-lock DNA nanodevice (DKL-DND) in response to acidic pH and ATP for on-demand activation and multimodal imaging guided combined tumour therapy. (A) Design of the DKL-DND. (B) Illustration of DKL-DND for multi-modal imaging guided combined tumour therapy.

tumour cells. The ingenious combination of these constructs in DKL-DND endows it with extraordinary performance in optical/magnetic resonance multimodal imaging guided gene/chemo/small molecule combined cancer therapy.

Characterization of DKL-DND

First, the Au@Ag@Au DSNPs were prepared *via* a layer-by-layer coating process. From transmission electron microscopy (TEM) characterization (Fig. 1A-a), 17 nm AuNPs are synthesized as the inner core, and then the uniform Au@Ag NPs are prepared with less free Ag nuclei using L-ascorbic acid (L-AA) as the reducing agent (Fig. 1A-b). The thickness of the Ag shell can be modulated by changing the amount of Ag^+ (Fig. S1A and S1B†). In particular, the Au@Ag NPs with a 2.0 nm Ag shell exhibits the best SERS enhancement effect using 4-MBA as a Raman signal molecule (Fig. S1C and S1D†), which is chosen for further experiments. Although Au@Ag NPs reveal superior optical properties, they still suffer from low stability, high toxicity and poor performance upon surface functionalization. Alternatively, a uniform layer of Au was further coated on Au@Ag NPs to obtain the Au@Ag@Au DSNPs through a sulfite-based epitaxial deposition protocol (Fig. 1A-c), which can efficiently prevent the galvanic replacement to improve the stability of Au@Ag NPs and further reduce the toxicity induced by released Ag^+.[34] Notably, the thickness of the Au shell is optimized to be ~1.25 nm (Fig. S2†). The energy-dispersive X-ray spectroscopy (EDX) mappings intuitively display the distribution of Au and Ag elements, indicating the formation of Au@Ag@Au DSNPs without any galvanic replacement reactions (Fig. S3†). It should be noted that the SERS signal of Au@Ag@Au DSNPs is significantly enhanced at 1590 cm^{-1} compared with bare AuNPs and Au@Ag NPs (Fig. 1B). As shown in the finite difference time domain (FDTD) simulation data (Fig. 1B, inset), the Au@Ag@Au DSNPs produce a large area of electric field enhancement and high electric field intensity. These results indicate the excellent Raman enhancement activity of Au@Ag@Au DSNPs, which can be attributed to the synergistic plasmonic interaction among the Au core, Ag shell and ultrathin Au shell. In addition, the stability of Au@Ag@Au DSNPs was evaluated *via* H_2O_2 etching (Fig. S4†). As expected, the ultrathin Au shell plays a significant role in protecting the Ag shell, which is beneficial for further biological applications.

Subsequently, by virtue of Au–S bonds, the thiolated HA hybrids were functionalized on Au@Ag@Au DSNPs. The amount of HA hybrids immobilized on each Au@Ag@Au DSNPs is quantified to be ~42 by fluorescence assay (Fig. S5†), which thus provide plentiful Dox-loading sites *via* intercalating into G–C base pairs. Finally, the MOF shell was coated through the coordination between TA and Mn^{2+}, which further served as the carrier to load Fuel strand *via* hydrogen bonding to obtain the DKL-DND. The fabricated DKL-DND exhibits an average size of 31 nm with a MOF shell of approximately 3.75 nm (Fig. 1A-d). As shown in Fig. 1C and S6,† the EDX mappings and X-ray photoelectron spectroscopy (XPS) spectra display the chemical

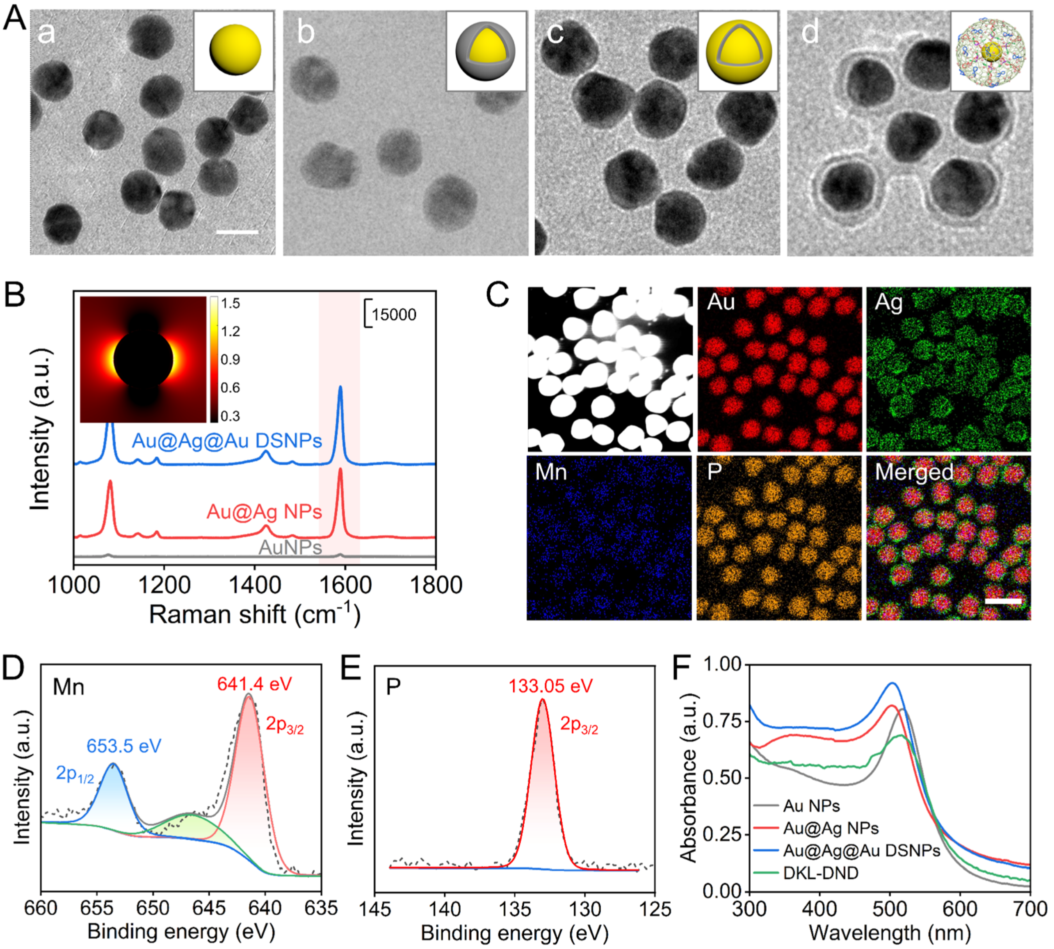

Fig. 1 Characterization of DKL-DND. (A) TEM images of (a) AuNPs, (b) Au@Ag NPs, (c) Au@Ag@Au DSNPs, and (d) DKL-DND. Scale bar: 20 nm. (B) SERS spectra measurements of AuNPs, Au@Ag NPs and Au@Ag@Au DSNPs using 4-MBA as a Raman signal molecule. (Inset) FDTD-simulated electric field distribution of Au@Ag@Au DSNPs with incident light of $\lambda = 633$ nm. (C) Elemental mapping of DKL-DND. Scale bar: 50 nm. XPS spectra of (D) Mn 2p and (E) P 2p in DKL-DND. (F) UV-vis spectra of AuNPs, Au@Ag NPs, Au@Ag@Au DSNPs and DKL-DND.

element composition (Au, Ag, Mn and P) of DKL-DND. In particular, Mn (641.4 eV and 653.5 eV) and P (133.05 eV) elements come from the Mn-TA network and DNA, respectively (Fig. 1D and E). In addition, Fig. S7† shows the Raman spectra of TA and DKL-DND. Compared with the pure TA, the characteristic peak at around 655 cm^{-1} appears, which can be attributed to the chelation of Mn^{2+} by the phenolic oxygen in TA.

The synthesis processes of DKL-DND were further characterized using UV-vis absorption spectra (Fig. 1F). The Au NPs present a localized surface plasmon resonance (LSPR) peak at 518 nm. After coating with an Ag layer, the corresponding LSPR peak is blue-shifted to 502 nm, and a weak absorption peak associated with the Ag plasmon resonance is observed at 395 nm, suggesting the formation of Au@Ag NPs. Compared with Au@Ag NPs, the characteristic absorption of Au@Ag@Au DSNPs red-shifts to 504 nm and the Ag peak at 395 nm is not changed. Furthermore, the characteristic peak of DKL-DND red-shifts to 516 nm due to the formation of the MOF shell. Both the particle sizes (Fig. S8A†) and ζ-potential value changes (Fig. S8B†) further confirm the fabrication of DKL-DND for each step. Notably, the DKL-DND demonstrates satisfactory stability since the MOF shell could protect DNA strands from nuclease degradation (Fig. S9†).

In vitro stimuli-responsive ability of DKL-DND and FL/SERS detection of miR-21

The proposed DKL-DND is composed of inner Dox/HA-DSNP probes and outer MOFs loaded with Fuel strands, in which the MOF shell operates as the pH-responsive lock and the Aptazyme works as the ATP-responsive lock. As the first stimulus, acidic pH in the lysosome (4.5–5.5, Key I) promotes the rapid dissociation of the MOF shell, releasing Mn^{2+}, TA and Fuel strand as well as the Dox/HA-DSNP probes. Subsequently, the high concentration of ATP in the cytoplasm (1–10 mM, Key II) induces the disassembly of HA hybrids to form ATP/Aptazyme complex, releasing the Hairpin-DSNPs and Dox (Fig. 2A).

First, the pH-responsive properties of DKL-DND were verified *via* inductively coupled plasma mass spectrometry (ICP-AES) analysis of the Mn element. Due to the dissociation of the MOF shell under acidic conditions, an extensive amount of

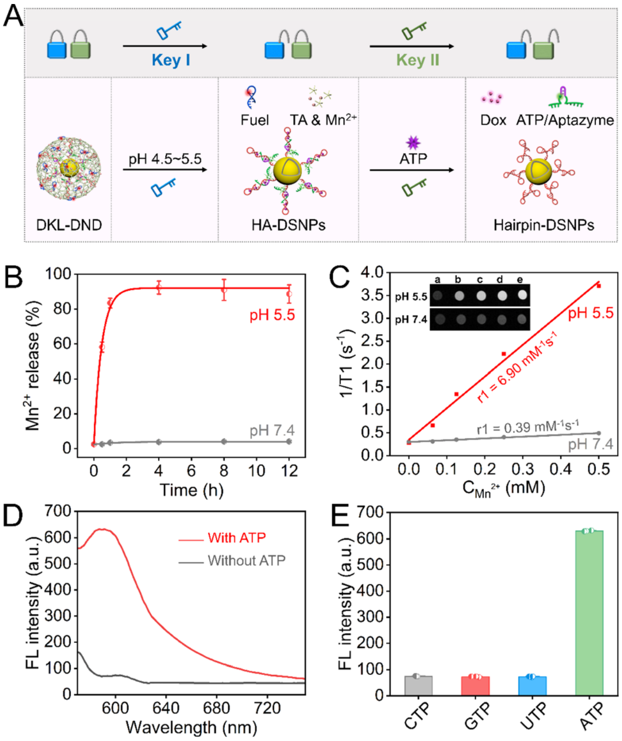

Fig. 2 *In vitro* stimuli-responsive ability of DKL-DND. (A) Cascaded activation of DKL-DND in response to acidic pH (Key I) and ATP (Key II). (B) Release efficiency of Mn^{2+} for DKL-DND under different pH conditions. (C) Plots of 1/T1 *vs.* DKL-DND concentrations. Inset: T1-MR images of DKL-DND with various concentrations under different pH conditions: (a) 0; (b) 0.0625 mM; (c) 0.125 mM; (d) 0.25 mM; and (e) 0.5 mM. (D) Fluorescence spectra of DKL-DND in the absence or presence of ATP (5 mM). (E) Specificity of DKL-DND in response to different nucleoside triphosphates (5 mM for each) under acidic pH. Error bars represent the standard deviation obtained from three independent assays.

Mn^{2+} release is observed within 1 h (reaching ~85%) when the DKL-DND is exposed to a weakly acidic environment (pH 5.5), whereas a small amount of Mn^{2+} is released from DKL-DND at pH 7.4 (Fig. 2B). The TEM image further verifies the acidic pH-controlled dissociation properties of DKL-DND (Fig. S10†). Moreover, the released Mn^{2+} could serve as the contrast agent for T1-weighted MRI. After incubating in a mildly acidic buffer (pH 5.5) for 4 h, the DKL-DND presents a concentration-dependent brightness effect, and the corresponding longitudinal relaxivity (r_1) is calculated to be 6.90, which is much higher than that in a neutral buffer (0.39) (Fig. 2C). These results indicate that the mildly acidic environment could cause an efficient decomposition of the MOF shell.

Subsequently, fluorescence assay was performed to investigate the ATP-responsive performance of DKL-DND in an acidic buffer (pH 5.5). The Aptazyme is labelled with a fluorophore (Rox) at the middle position. If the DKL-DND is in a locked state, the Rox-tagged Aptazyme is close to the surface of Au@Ag@Au DSNPs, and its fluorescence is quenched. In contrast, the introduction of ATP initiates the disassembly of HA hybrids, making the fluorophore Rox away from Au@Ag@Au DSNPs and producing a fluorescent signal output. As expected, compared with the control group without ATP, the fluorescence signal of Rox significantly increases with the addition of 5 mM ATP, suggesting the successful disassembly of HA hybrids (Fig. 2D). In contrast, UTP, CTP, or GTP induces little fluorescence change, demonstrating the high specificity of DKL-DND towards ATP under weakly acidic pH (Fig. 2E). In addition, since the concentration of ATP is much higher than that of other adenine nucleotides (ADP and AMP) under physiological conditions, it will be more successful at competing with ADP and AMP despite their similar binding constants.[35] Therefore, the DKL-DND exhibits an obvious response to the dual stimuli of acidic pH and ATP, which lays a foundation to precisely control the operation of the DNA nanodevice in cancer cells.

After the cascaded response of weakly acidic pH and ATP, the target miR-21 could trigger a continuous CHA reaction between the unlocked Hairpin-DSNPs and Fuel strand, forming multiple HF-DSNPs (Fig. S11A†). The feasibility of DKL-DND for FL/SERS dual-mode detection of miR-21 was investigated (Fig. S11B and S11C†). The reaction pathways of CHA and Aptazyme-catalysed cleavage are characterized by native polyacrylamide gel electrophoresis (PAGE) (Fig. S12A†), and the concentration of Mn^{2+} was also investigated for the Aptazyme-catalysed cleavage reaction (Fig. S12B†). Under the optimal conditions (Fig. S13†), miR-21 with different concentrations was detected in the presence of ATP under weakly acidic conditions (pH 5.5) using FL and SERS modes, respectively. For FL detection, a good linear trend is obtained between the fluorescence intensity at 675 nm and the logarithm of miR-21 concentration ranging from 250 pM to 75 nM, and the limit of detection (LOD) is calculated to be 0.74 pM (3σ) (Fig. S14A†). For SERS detection, with increasing the miR-21 concentration from 0.1 fM to 1 nM, the SERS intensity of Cy5 at 1595 cm^{-1} increases accordingly with a LOD as low as 0.14 aM (Fig. S14B†). The linear range and LOD of this method are comparable to previously reported strategies for miRNA detection (Table S2†). Also, the SERS signals at 1595 cm^{-1} from 11 random spots are recorded, and the relative standard deviation (RSD) is calculated to be 4.74%, indicating the excellent reproducibility of DKL-DND for SERS detection of miR-21 (Fig. S14C and S14D†). In addition, this DNA nanodevice enables the highly selective detection of miR-21, and exhibits excellent anti-interference ability (Fig. S14E, S14F and S15†).

Dual-mode imaging of intracellular miR-21

The intracellular imaging was conducted using MCF-7 cells with a high miR-21 expression profile (Fig. 3A). To monitor the internalization pathway of DKL-DND, the co-localization experiments were first performed, in which the red/green/blue fluorescence was derived from Cy5-labelled Fuel strand, Lyso-Tracker Red-stained lysosomes, and Hoechst 33342-stained nucleus, respectively (Fig. 3B). The colocalization degree of DKL-DND and lysosome reaches the highest at 3 h. As incubation proceeds, Pearson's correlation gradually decreases and the poor colocalization indicates the successful escape of loaded cargoes from lysosomes. This result is consistent with the reported study that the coating of metal-phenolic networks

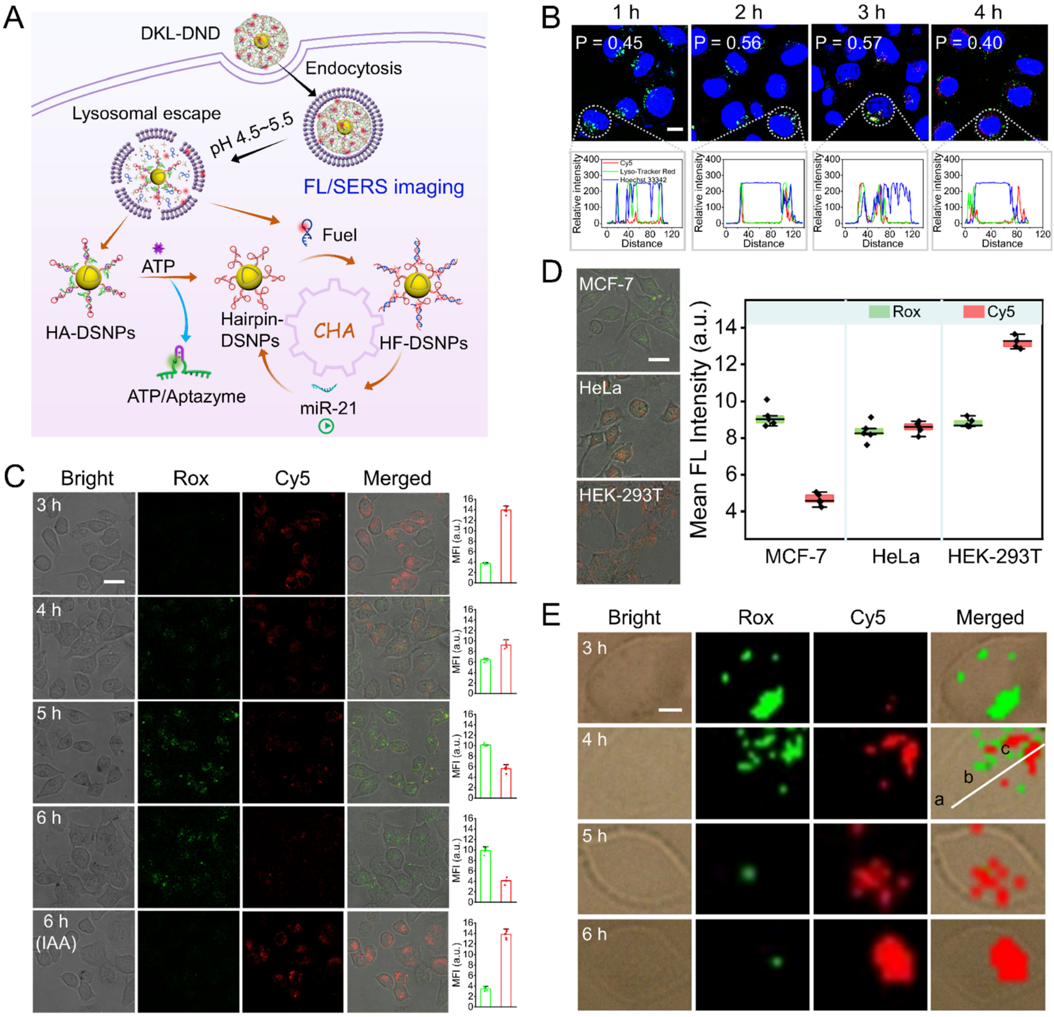

Fig. 3 Dual-mode imaging of intracellular miR-21. (A) The intracellular behaviours of DKL-DND for dual-mode imaging of miR-21. (B) Cellular co-localization assay after incubation with Cy5-labelled DKL-DND (red) for different time points, and Pearson's correlation of Cy5-labelled DKL-DND and lysosome at different incubation times of 5 cells. LysoTracker Red (green) for lysosome, and Hoechst 33342 (blue) for nuclei. Scale bar: 10 μm. Hoechst 33342 (blue): Ex = 405 nm, Em = 415–470 nm. LysoTracker Red (green): Ex = 577 nm, Em = 585–630 nm. Cy5 (red): Ex = 635 nm, and Em = 650–750 nm. (C) CLSM images of DKL-DND for miR-21 analysis in MCF-7 cells at different times. Rox-labelled Aptazyme (green) for ATP, and Cy5-labelled Fuel strand (red) for miR-21. Rox (green): Ex = 587 nm and Em = 595–630 nm. (D) CLSM images and corresponding fluorescence intensity for *in situ* analysis of miR-21 in MCF-7, HeLa and HEK-293T cells, respectively. Scale bars in (C and D): 25 μm. (E) SERS images of DKL-DND for miR-21 analysis in MCF-7 cells at different times. Scale bar: 5 μm. Error bars represent the standard deviation obtained from three independent assays.

can cause the osmotic rupture of the endo/lysosome membrane *via* the "proton-sponge effect", which thus facilitates the lysosomal escape behaviour of nanoparticles.[33]

Further, the capability of DKL-DND for intracellular FL/SERS dual-mode imaging of miR-21 was studied. For FL imaging, the confocal laser scanning microscope (CLSM) images were acquired from different incubation time points (Fig. 3C). The green fluorescence from Rox-labelled Aptazyme gradually increases with increasing incubation time, indicating the disassembly of HA hybrids induced by ATP recognition. Meanwhile, the red fluorescence from Cy5-labelled Fuel strand associated with miR-21-triggered CHA gradually decreases and reaches the minimum at 6 h, which thus is chosen as the optimal time for intracellular microRNA imaging. To further demonstrate the ATP-specific responsiveness, the MCF-7 cells were pretreated with iodoacetic acid (IAA) to down-regulate the ATP level *via* inhibiting glycolysis. After incubation for 6 h, the DKL-DND doesn't respond to intracellular miR-21. Thus, the overexpressed miR-21 in MCF-7 cells can effectively trigger the CHA reaction for signal output only at the acidic pH and high concentration of ATP conditions. Flow cytometry results also confirm these phenomena (Fig. S16†). In addition, this DNA nanodevice is able to well monitor the varied expressions of intracellular microRNAs (Fig. S17†).

To evaluate the miR-21-imaging capability of DKL-DND in different types of cell lines, the breast cancer cells (MCF-7), human cervical cancer cells (HeLa) and human embryonic kidney cells (HEK-293T) were respectively incubated with DKL-DND for 6 h (Fig. 3D). The green fluorescence signals which beamed back from Rox-labelled Aptazyme associated with ATP are almost the same in MCF-7, HeLa, and HEK-293T cells, which can be attributed to the high concentrations of ATP in those cells (4.72 mM in MCF-7 cells, 5.36 mM in HeLa cells, and 3.39 mM in HEK-293T cells) that are sufficient to cause the disassembly of HA hybrids and eliminate the differences in activation processes in different cell lines (Fig. S18†). As expected, the MCF-7 cells with high expression of miR-21 exhibit the weakest Cy5 fluorescence signals, while a much stronger signal is observed in HeLa cells which have a trace amount of miR-21 expression. The HEK-293T cells, known with low miR-21 expression, demonstrate the strongest Cy5 fluorescence signal. These findings agree well with previous studies,[36] and show good consistency with the results from qRT-PCR analysis (Fig. S19†).

For SERS imaging of miR-21, the SERS intensity increases for Cy5 and decreases for Rox as the incubation time proceeded (Fig. 3E). We further acquire the SERS spectra of Cy5 from different locations in MCF-7 cells (Fig. S20†). Compared with the nucleus and surrounding environment regions, the significantly high SERS intensity is observed within the cytoplasm, indicating the performance of CHA triggered by miR-21 most within the cytoplasm.

Evaluation of antitumour therapy *in vitro*

Because of the precise cascaded activation properties towards acidic pH and ATP, the proposed DKL-DND has the ability to collect and process biological signals to adjust their behaviour within cancer cells, which thus can serve as an ideal nanocarrier to deliver multiple anticancer drugs and effectively prevent side effects caused by premature leakage during drug delivery. It is well known that Dox can intercalate into the G–C base pairs of the DNA duplex.[37] Thus, the as-prepared DKL-DND with a large amount of HA hybrids can provide plentiful Dox-loading sites for chemotherapy. In addition, the outer MOF shell could be dissociated under acidic pH to release Mn^{2+} and TA. The released Mn^{2+} can be used as the Aptazyme cofactors for cleaving EGR-1 mRNA to activate gene therapy, which can further promote chemosensitivity as well as inhibit cell proliferation and migration. Meanwhile, TA as a polyphenolic small molecule inhibitor is particularly effective for anti-metastasis.[38] Therefore, it is reasonable to suppose that the DKL-DND will be useful to inhibit proliferation, and migration and promote apoptosis of tumour cells *via* combination treatment (Fig. 4A).

Since the fluorescence of Dox can be quenched after interacting with the DNA duplex, we first determined the Dox loading and release capacity of DKL-DND by fluorescence assay (Fig. S21†). Moreover, we further validated the release behaviour of Dox at the cellular level *via* CLSM imaging (Fig. 4B). The fluorescence signal of Dox released from DKL-DND increases when the incubation period is lengthened. And the gradual overlap of red (Dox) and blue (nucleus) fluorescence indicates the intracellular diffusion behaviour of Dox. Thus, the loaded Dox can be efficiently released in the cytoplasm, followed by gradually entering the nucleus for chemotherapy.

To evaluate the Aptazyme-mediated EGR-1 mRNA silencing in the presence of Mn^{2+} coactivators, the qRT-PCR assay was performed to analyse the relative expression levels of EGR-1 mRNA within MCF-7 cells (Fig. 4C). To expel a possible Dox interference, here DKL-DND was prepared using catalytically active Aptazyme without Dox loading (denoted as A-DKL-DND). As expected, the expression of EGR-1 mRNA is obviously decreased by 46.39% through treated with A-DKL-DND (sample c), while the catalytically inactive N-DKL-DND (prepared using catalytically inactive Aptazyme without Dox loading) (sample b) shows almost identical readings compared with PBS control (sample a). The down-regulation capability of A-DKL-DND on EGR-1 protein expression is further measured *via* western blot (WB) analysis (Fig. 4D), which agrees well with the qRT-PCR data of its mRNA codon, indicating the efficient gene regulation ability of DKL-DND.

Next, we investigated whether the released TA from MOF shells and the silencing of EGR-1 mRNA could inhibit cell migration *via* a wound-healing assay (Fig. 4E and S22†). After incubation for 24 h, the relative mobilities of N-DKL-DND and A-DKL-DND treated groups are 16.25% and 6.81%, respectively. Its inhibition effect is witnessed compared with the PBS-treated control group (22.49%). More importantly, the A-DKL-DND-treated group exhibits the best suppression effect, indicating a synergistic inhibition from TA and Aptazyme for tumour cell migration.

Given the excellent drug release and efficient gene regulation ability of DKL-DND, the anti-cancerous ability of this combined therapy nanoplatform was investigated. First, the cell viability of MCF-7 cells treated with PBS, N-DKL-DND, A-DKL-DND, free Dox, D-DKL-DND (prepared using catalytically inactive Aptazyme with Dox) and DKL-DND for 48 h was measured *via* CCK-8 assay, respectively (Fig. 4F). The proliferation of MCF-7 cells is inhibited by 54.04% for DKL-DND treatment (sample f), which is much higher than those of A-DKL-DND (22.67%, sample c), free Dox (24.09%, sample d) and D-DKL-DND (28.12%, sample e) treated cells at the same concentration (5 nM), proving the effectiveness of combined therapy. To analyse the cell apoptosis rate, the flow cytometry assay was further carried out using the annexin V-APC/7-AAD staining kit (Fig. 4G). Clearly, after incubation with A-DKL-DND (sample c), free Dox (sample d) and D-DKL-DND (sample e), the MCF-7 cells undergo the cell apoptosis rates of 11.63%, 11.79% and 14.35%, respectively, while the apoptosis rate of DKL-DND treated cells (sample f) is up to 27.3%, confirming the higher therapeutic efficiency than those of mono-treatment systems. In addition, the live/dead cell double-staining experiments were carried out to visually assess the therapy efficacy of different treatments, in which the live and dead cells presented green and red fluorescence, respectively (Fig. 4H). As expected, the therapeutic efficacy of DKL-DND results in the highest toxicity to MCF-7 cells, which is in agreement with the above results.

In vivo antitumour efficacy of DKL-DND

Encouraged by the excellent *in vitro* cell proliferation inhibitory effect, the *in vivo* therapeutic potential against MCF-7 tumour-bearing mice was further investigated. First, the hemolysis assay demonstrates an excellent biostability of DKL-DND within

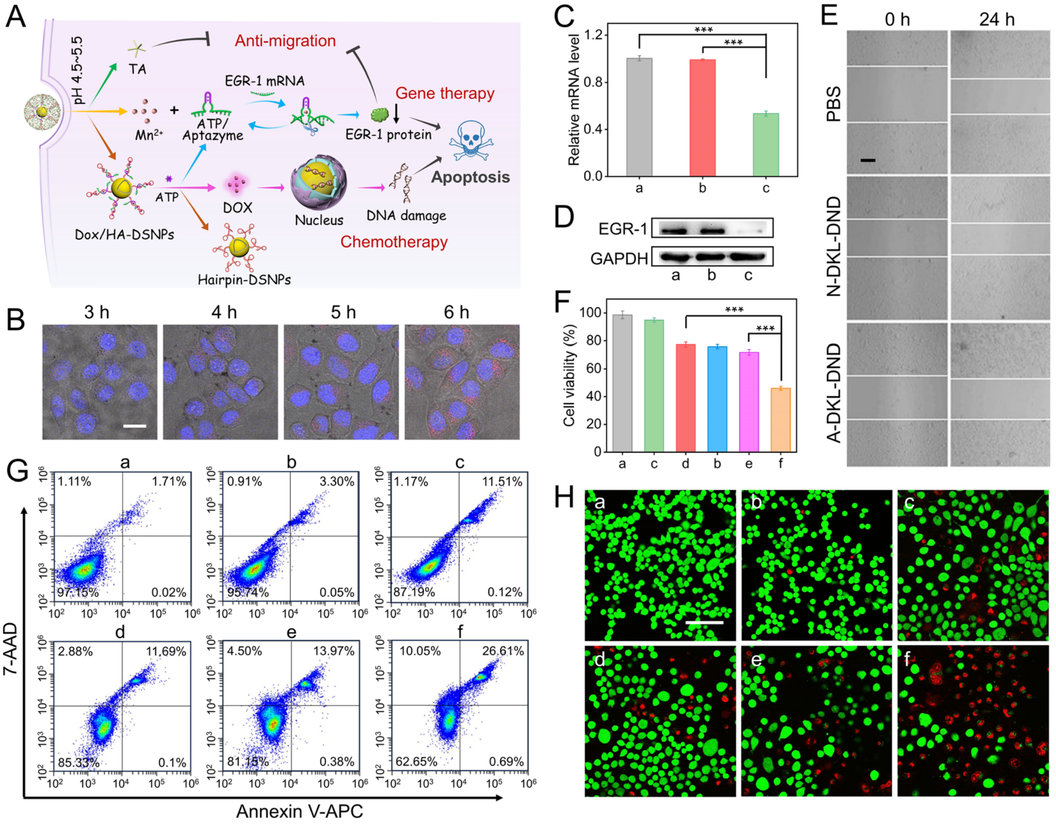

Fig. 4 *In vitro* antitumor therapy of DKL-DND. (A) Antitumor performance of DKL-DND *via* a combination of chemo-gene therapy with TA-assisted anti-migration. (B) Time course CLSM images of Dox released from DKL-DND in MCF-7 cells at indicated time points. Scale bar: 20 μm. (C) qRT-PCR analysis of EGR-1 mRNA and (D) western blot analysis of EGR-1 proteins in MCF-7 cells incubated with (a) PBS, (b) N-DKL-DND, and (c) A-DKL-DND. (E) Wound healing abilities of MCF-7 cells with different treatments. Scale bar: 100 μm. (F) Cell viability, (G) cell apoptosis, and (H) Live/Dead cell staining assay of MCF-7 cells treated with (a) PBS, (b) N-DKL-DND, (c) A-DKL-DND, (d) free Dox, (e) D-DKL-DND, and (f) DKL-DND, respectively. The final concentration of DKL-DND is 5 nM. Scale bar in (H): 100 μm. Error bars represent the standard deviation obtained from three independent assays.

blood (Fig. S23†). Next, the dynamic accumulation behaviours of DKL-DND were monitored using an animal imaging system (Fig. 5A). The Cy5-labelled free Fuel strand could be metabolized quickly *in vivo* after intravenous injection for 12 h. In comparison, the fluorescence signal of DKL-DND-treated mice gradually enhances with the prolongation of time and reaches a maximum at 12 h and sustains for 24 h. Notably, the corresponding average fluorescence intensity at the tumour site from DKL-DND-treated mice is higher than that injected with free Fuel strand (Fig. S24†). This is because the protective action of MOFs prolongs the blood circulation of DNA structures, which facilitates tumour accumulation through the typical enhanced permeability and retention (EPR) effect. After continuous imaging, the tumour and major organs of free Fuel strand- and DKL-DND-treated mice are obtained for further *ex vivo* fluorescence imaging, and the quantitative analysis results also support the above statement (Fig. S25†). Obviously, the DKL-DND shows excellent biocompatibility, biostability and efficient accumulation ability at tumour sites after intravenous injection, which thus ensures its combined therapeutic effects.

Since the released Mn^{2+} could be utilized as the contrast agent, the *in vivo* T1-weighted MRI of tumours was acquired for tumour diagnosis by intravenous injection of DKL-DND into mice (Fig. 5B). The tumour site is clearly whitened after intravenous injection of DKL-DND for 12 h compared to that prior to injection, indicating that DKL-DND is a promising potential nanoplatform for multimodal imaging-guided cancer combined therapy. Subsequently, the inductively coupled plasma mass spectrometry (ICP-MS) analysis of the Mn element was used to monitor the distribution of DKL-DND in MCF-7 tumour-bearing mice (Fig. S26†). The Mn element is mainly distributed in the liver, spleen and kidney, and significantly decreases in these organs with the extended post-injection time, indicating that DKL-DND could be metabolized without long-term toxicity.

Based on the satisfactory antitumor efficacy *in vitro* and the excellent tumour accumulation of DKL-DND, the synergistic anticancer efficacy *in vivo* was further evaluated against tumour models. When the tumour volume reached ~80 mm^3, the MCF-7 tumour-bearing BALB/c mice were randomly divided into six groups (4 mice per group) and respectively treated with (I) PBS, (II) N-DKL-DND, (III) A-DKL-DND, (IV) free Dox, (V) D-DKL-DND and (VI) DKL-DND *via* tail vein injection according to the time schedule (Fig. 5C). During the whole therapeutic process, the tumour volume was measured every 2 days using a vernier caliper. As shown in Fig. 5D, the DKL-DND treated group

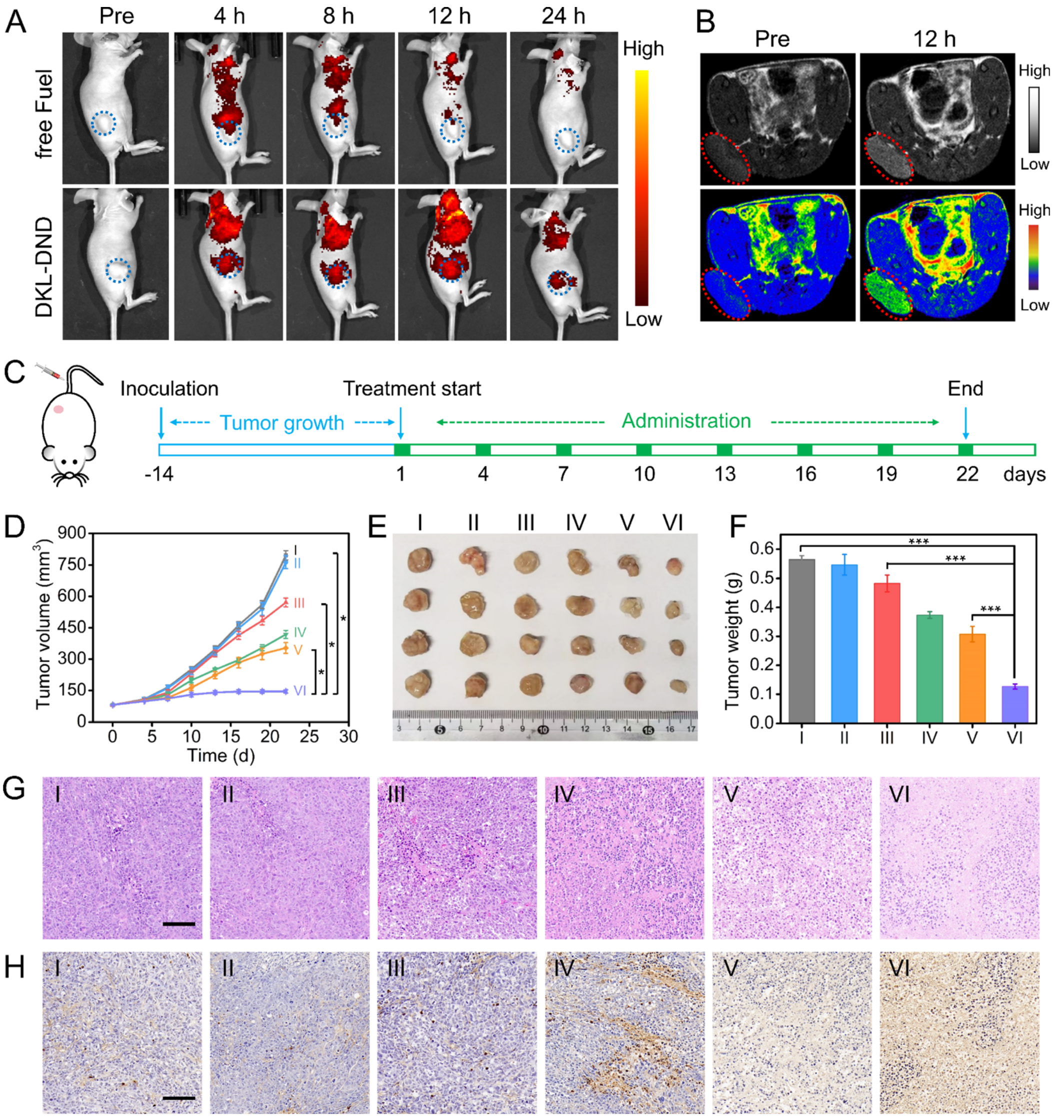

Fig. 5 *In vivo* antitumour behaviours of DKL-DND. (A) Dynamic biodistribution of free Fuel strand and DKL-DND in MCF-7 tumour-bearing nude mice at different times post-injection, respectively. (B) T1-weighted MR images of tumour-bearing mice before and after intravenous injection of DKL-DND for 12 h. (C) Time scheme of tumour treatment *in vivo* for DKL-DND. (D) Tumour volume evolution curves during therapy. (E) Photos and (F) corresponding weights of dissected tumours from mice with different treatments. (G) H&E and (H) TUNEL staining images of tumour tissues from different treatment groups. From I to VI: (I) PBS, (II) N-DKL-DND, (III) A-DKL-DND, (IV) free Dox, (V) D-DKL-DND and (VI) DKL-DND. Scale bars: 100 μm. Error bars represent the standard deviation obtained from three independent assays.

exhibits the best tumour-suppressing effects, suggesting improved anticancer ability *via* combined therapy. The mouse body weights were also recorded to evaluate the safety of DKL-DND (Fig. S27†). Except for the free Dox treated group, the body weight of other groups gradually increases during different treatments, indicating the very little systemic toxicity of this DNA nanodevice. Moreover, after treatment, the tumour tissues in different groups were collected and weighed. The morphology and mass of tumours exhibit a significant difference between DKL-DND and mono-treatment groups, which summed up all the therapeutic benefits that DKL-DND can provide during tumour growth inhibition research (Fig. 5E and F). In addition, the expression level of EGR-1 protein in excised tumours from different treatment groups was analysed using WB assay (Fig. S28†), in which both A-DKL-DND and DKL-DND could downregulate EGR-1 protein expression, indicating the efficient *in vivo* gene silencing capacity of Aptazyme.

The synergistic therapy effect of DKL-DND was further demonstrated using hematoxylin and eosin (H&E) and terminal deoxynucleotidyl transferase deoxyuridine triphosphate (dUTP) nick-end labelling (TUNEL) staining assay at the end of treatment (Fig. 5G and H). Meanwhile, the major organs (heart, liver, spleen, lungs, and kidney) in different treatment groups were collected to investigate the toxicity of different treatments by H&E staining (Fig. S29†). The histological analysis shows no obvious tissue damage after being treated with DKL-DND for 21 days, while free Dox causes an observable disorganization in the heart, further assuring the high biosafety of the constructed

DNA nanodevice. In addition, the blood biochemistry analysis indicates that the DKL-DND causes little effect on liver and kidney functions (Fig. S30†). Therefore, the fabricated DKL-DND can not only enable real-time monitoring of tumour treatment *via in vivo* imaging but also enhance the antitumor efficacy with low systemic toxicity.

Conclusions

In conclusion, we have devised an integrated dual-key-and-lock DNA nanodevice for accurate diagnosis and combined therapy of cancers, and its advantages can be summed up as such. (1) On-demand activation. The endogenous pH/ATP-responsive locks are introduced to improve the spatial specificity of the DNA nanodevice and minimize the nonspecific activation during assembly and delivery. (2) *In situ* multimodal imaging for cancer diagnosis. FL/SERS dual-mode imaging of intracellular microRNA provides the complementary advantages of these two technologies for accurate diagnosis. Benefitting from the CHA-based signal amplification and endogenous activation endowed spatial selectivity, it is easy to achieve enhanced signal-to-background ratios and improved detection sensitivity. Meanwhile, Mn^{2+} decomposed from DKL-DND serves as a T1-weighted contrast agent for MRI to obtain the multiscale tumour-related diagnosis information *via* combining with optical imaging tools. (3) Combined therapy and reduced off-site delivery. This DNA nanodevice produces both excellent chemotherapy and the gene silencing effect in specific tumour microenvironments, realizing an enhanced anti-tumour ability *in vitro* and *in vivo*. Meanwhile, TA as a small molecule inhibitor is particularly effective for anti-metastasis. Overall, our proposed DNA nanodevice provides a promising nanoplatform for integrated diagnosis and treatment with improved anti-interference ability, thus offering a new way for nucleic acid-based precise medicine and personalized theragnostic systems.

Experimental

Preparation of DKL-DND

First, Dox was added into the prepared HA-DSNP solution with a molar ratio of 400 : 1, followed by incubation at 25 °C for 24 h to prepare the Dox/HA-DSNPs. Then, 100 μL of the prepared Dox/HA-DSNPs was added to 2 mL of ultrapure water under vigorous stirring and subsequently sonicated for 2 min. A portion of 2.5 μL TA (20 mg mL^{-1}) and 2.5 μL of $MnCl_2$ (20 mg mL^{-1}) were rapidly added to the solution in sequence. After stirring for 5 min, 110 μL of phosphate buffer (0.2 M, pH 7.4) was added to the mixture, followed by sonication for 5 min and vigorous stirring at 30 °C in the dark for 2 h. The resulting Dox/HA-DSNPs@MOFs was collected by centrifugation and then washed with 1× PBS (pH 7.4). Afterwards, the obtained Dox/HA-DSNPs@MOFs was incubated with Fuel strand for 30 min at room temperature, followed by adding 1× PBS (pH 7.4) with an incubation period of 30 min. Finally, the Dox/HA-DSNPs@MOFs/Fuel, also called DKL-DND, was collected *via* centrifugation and stored in 1× PBS (pH 7.4) at 4 °C. In addition, different formulations of DKL-DND were constructed as follows: the A-DKL-DND was prepared using catalytically active Aptazyme without Dox loading, the N-DKL-DND was prepared using catalytically inactive Aptazyme without Dox loading, and the D-DKL-DND was prepared using catalytically inactive Aptazyme with Dox. In this work, both A-DKL-DND and D-DKL-DND were single-modal treatment groups, which served as the control experiments.

Intracellular imaging

Confocal laser scanning microscope (CLSM) imaging. An amount of 10^5 cells were seeded in a confocal dish (30 mm × 15 mm) and cultured at 37 °C for 24 h. Then, the cells were treated with DKL-DND with a final concentration of 5 nM for different time periods. Afterwards, the medium was removed and the cells were washed three times with 1× PBS (pH 7.4). Finally, the FL images were collected on an inverted confocal microscope (Leica TCS SP8, Germany). To regulate the ATP level, the MCF-7 cells were pretreated with iodoacetic acid (IAA) (100 μM) for 4 h before incubation with DKL-DND. To measure the expression levels of intracellular miR-21, the miR-21 mimics and anti-miR-21 sequences were transfected into MCF-7 cells for 4 h, respectively. For the colocalization experiment, the cells were treated with Cy5-labelled DKL-DND (without Rox) for different time periods, and further incubated with the DMEM containing Lyso-Tracker Red and Hoechst 33342 for an additional 30 min at 37 °C to stain the lysosomes and nuclei, respectively. The excitation wavelengths of Lyso-Tracker Red, Hoechst 33342, Dox, Rox and Cy5 were 577, 405, 488, 587 and 635 nm, respectively. Their FL signals were obtained using 585–630 nm, 415–470 nm, 540–620 nm, 595–630 nm and 650–750 nm channels, respectively.

SERS imaging. The MCF-7 cells (10^5 cells per well) were seeded in a glass-bottom dish (35 mm × 10 mm) and cultured at 37 °C for 24 h. Then, the cells were treated with DKL-DND for different time periods. The final concentration of DKL-DND was 5 nM. After the removal of the medium, the cells were washed with 1× PBS three times. Finally, the Raman images were collected on a Raman microscope with a 633 nm laser (50× objective lens) (Renishaw inVia, UK). The laser power and the accumulation were set as 50% and 1, respectively.

Cell apoptosis assessment

The MCF-7 cells were seeded in a 12-well plate at a density of 10^5 cells per well and cultured for 24 h. Then, the medium was removed and the cells were treated with fresh DMEM containing PBS, N-DKL-DND, A-DKL-DND, free Dox, D-DKL-DND and DKL-DND, respectively. The final concentration of DKL-DND was 5 nM. After 48 h incubation, the cells were washed with 1× PBS and stained with Annexin V-APC/7-AAD (MultiSciences (LIANKE) Biotech, Co., Ltd., Hangzhou). The apoptosis was quantitatively assessed using flow cytometry (Beckman Coulter FC500, USA) by counting 30 000 events.

In vivo tumour therapy

When the tumour size reached ~80 mm^3, the MCF-7 tumour-bearing mice were randomly divided into six groups (4 mice per group). Then, those mice in different groups were intravenously injected with PBS, N-DKL-DND, A-DKL-DND, free Dox, D-DKL-DND and DKL-DND, respectively. The therapeutic agents were injected every third day for eight times. During the treatment, the variation of tumour size and mice body weight was monitored. Finally, the mice were sacrificed, and the tumours and main organs (heart, liver, spleen, lungs and kidney) were removed for further histopathology evaluation at the end of treatment.

Statistical analysis

The experimental data were presented as mean ± standard deviation. The statistical analysis was performed by the Student's *t*-test for comparison of two groups using the GraphPad Prism software (Version 5, GraphPad Software, Inc., La Jolla, USA). And the statistical significance was defined by an asterisk ($^*p < 0.05$, $^{***}p < 0.001$).

Data availability

The data that support the findings of this study are available in the ESI† of this article.

Author contributions

S. B. and S. Y. designed the present work. S. Y. performed most experiments, analyzed the data and wrote the manuscript. J. Z. and X. X. characterized the DNA nanomaterials. J. Z., S. B. and J. X. participated in the data analyses and edited the manuscript.

Conflicts of interest

The authors declare no competing interests.

Acknowledgements

The authors greatly appreciate the financial support from the National Natural Science Foundation of China (No. 22174061 and 22076087), the Taishan Scholar Foundation of Shandong Province (No. tstp20230623), and the Jiangsu Funding Program for Excellent Postdoctoral Talent (No. 20220ZB22).

Notes and references

1 M. Tang, B. Chen, H. Xia, M. Pan, R. Zhao, J. Zhou, Q. Yin, F. Wan, Y. Yan, C. Fu, L. Zhong, Q. Zhang and Y. Wang, *Nat. Commun.*, 2023, **14**, 5888.
2 G.-F. Luo, W.-H. Chen, X. Zeng and X.-Z. Zhang, *Chem. Soc. Rev.*, 2021, **50**, 945.
3 F. Tian, S. Zhou, S. Xie, Z. Zhang, L. Peng, L. Jiang, Z. Wang, Z. Nie and Y. Huang, *Chem. Sci.*, 2023, **14**, 12182.
4 Y. Zhao, S. Cao, Y. Wang, F. li, L. Lin, L. Guo, F. Wang, J. Chao, X. Zuo, Y. Zhu, L. Wang, J. Li and C. Fan, *Nat. Mach. Intell.*, 2023, **5**, 980–990.
5 F. Li, J. Li, B. Dong, F. Wang, C. Fan and X. Zuo, *Chem. Soc. Rev.*, 2021, **50**, 5650.
6 H. Chen, W. Xu, H. Shi, Y. Qiao, X. He, J. Zheng, S. Zhou, X. Yang, K. Wang and J. Liu, *Angew. Chem., Int. Ed.*, 2023, **62**, e202301559.
7 Y. Xie, H. Li, L. Xu, H. Zou, X. Wang, X. He, Q. Tang, Y. Zhou, X. Zhao, X. Chen, H. Liu, J. Pu, D. Luo and P. Liu, *Adv. Mater.*, 2023, **35**, 2208546.
8 W. Wang, Y. Gao, Y. Chen, W. Wang, Q. Li, Z. Huang, J. Zhang, Q. Xiang and Z.-S. Wu, *Adv. Sci.*, 2022, **9**, 2203698.
9 A. Ishaqat, X. Zhang, Q. Liu, L. Zheng and A. Herrmann, *J. Am. Chem. Soc.*, 2023, **145**, 12465–12474.
10 Z. Zhou, N. Lin, Y. Ouyang, S. Liu, Y. Zhang and I. Willner, *J. Am. Chem. Soc.*, 2023, **145**, 12617–12629.
11 Z. Wang, Y. Zhang, L. Wu, J. Chen, S. Xie, J. He, Q. Zhang, H. Chen, F. Chen, Y. Liu, Y. Zhang, Y. Zhuo, N. Wen, L. Qiu and W. Tan, *Angew. Chem., Int. Ed.*, 2023, **62**, e202307656.
12 S. Huang, C. Ma, J. Lin, W. Wang, Y. Xu, X. Wu, J.-R. Zhang and J.-J. Zhu, *CCS Chem.*, 2020, **2**, 1231–1244.
13 S. Li, H. Zhang, M. Zhu, Z. Kuang, X. Li, F. Xu, S. Miao, Z. Zhang, X. Lou, H. Li and F. Xia, *Chem. Rev.*, 2023, **123**, 7953–8039.
14 F. Yin, H. Zhao, S. Lu, J. Shen, M. Li, X. Mao, F. Li, J. Shi, J. Li, B. Dong, W. Xue, X. Zuo, X. Yang and C. Fan, *Nat. Nanotechnol.*, 2023, **18**, 677–686.
15 Q. Liu, Y. Huang, Z. Li, L. Li, Y. Zhao and M. Li, *Angew. Chem., Int. Ed.*, 2023, **62**, e202214958.
16 D. Yi, H. Zhao, J. Zhao and L. Li, *J. Am. Chem. Soc.*, 2023, **145**, 1678–1685.
17 Z. Di, J. Zhao, H. Chu, W. Xue, Y. Zhao and L. Li, *Adv. Mater.*, 2019, **31**, 1901885.
18 A. M. Yoshikawa, A. E. Rangel, L. Zheng, L. Wan, L. A. Hein, A. A. Hariri, M. Eisenstein and H. T. Soh, *Nat. Commun.*, 2023, **14**, 2336.
19 A. Ishaqat, X. Zhang, Q. Liu, L. Zheng and A. Herrmann, *J. Am. Chem. Soc.*, 2023, **145**, 12465–12474.
20 Y. Fan, Y. Zhou, M. Lu, H. Si, L. Li and B. Tang, *Research*, 2021, DOI: 10.34133/2021/9862876.
21 Z. Yang, B. Liu, T. Huang, M. Sun, T. li, W.-J. Duan, M.-M. Li, J.-X. Chen, Z. Dai and J. Chen, *Chem. Sci.*, 2022, **13**, 14373.
22 C.-C. Hsu, Y. Yang, E. Kannisto, X. Zeng, G. Yu, S. K. Patnaik, G. K. Dy, M. E. Reid, Q. Gan and Y. Wu, *ACS Nano*, 2023, **17**, 8108–8122.
23 H. Wang, Y. He, J. Wei, H. Wang, K. Ma, Y. Zhou, X. Liu, X. Zhou and F. Wang, *Angew. Chem., Int. Ed.*, 2022, **61**, e202115489.
24 Q. Li, X. Ge, J. Ye, Z. Li, L. Su, Y. Wu, H. Yang and J. Song, *Angew. Chem., Int. Ed.*, 2021, **60**, 7323–7332.
25 C. Zong, M. Xu, L.-J. Xu, T. Wei, X. Ma, X.-S. Zheng, R. Hu and B. Ren, *Chem. Rev.*, 2018, **118**, 4946–4980.
26 Y. Tan, J. Zhou, X. Xing, J. Wang, J. Huang, H. Liu, J. Chen, M. Dong, Q. Xiang, H. Dong and X. Zhang, *Anal. Chem.*, 2023, **95**, 11236–11242.
27 L. Pang, X. Tang, L. Yao, L. Zhou, S. Hu, S. Zhao and L. Zhang, *Chem. Sci.*, 2023, **14**, 3070.
28 Z. Lv, M. Huang, J. Yang, P. Li, L. Chang, Q. Tang, X. Chen, S. Wang, C. Yao, P. Liu and D. Yang, *Adv. Mater.*, 2023, **35**, 2300823.

29 K. Ma, W. Xie, W. Liu, L. Wang, D. Wang and B. Z. Tang, *Adv. Funct. Mater.*, 2021, **31**, 2102645.

30 R. Wang, W. He, X. Yi, Z. Wu, X. Chu and J.-H. Jiang, *J. Am. Chem. Soc.*, 2023, **145**, 17926–17935.

31 R. Liu, S. Zhang, T.-T. Zheng, Y.-R. Chen, J.-T. Wu and Z.-S. Wu, *ACS Nano*, 2020, **14**, 9572–9584.

32 Y. Zhang, Y. Zhang, X. Zhang, Y. Li, Y. He, Y. Liu and H. Ju, *Chem. Sci.*, 2020, **11**, 6289.

33 J. Chen, J. Li, J. Zhou, Z. Lin, F. Cavalieri, E. Czuba-Wojnilowicz, Y. Hu, A. Glab, Y. Ju, J. J. Richardson and F. Caruso, *ACS Nano*, 2019, **13**, 11653–11664.

34 H. Liu, T. Liu, L. Zhang, L. Han, C. Gao and Y. Yin, *Adv. Funct. Mater.*, 2015, **25**, 5435–5443.

35 B. Xiao, M. J. Sanders, E. Underwood, R. Heath, F. V. Mayer, D. Carmena, C. Jing, P. A. Walker, J. F. Eccleston, L. F. Haire, P. Saiu, S. A. Howell, R. Aasland, S. R. Martin, D. Carling and S. J. Gamblin, *Nature*, 2011, **472**, 230–233.

36 M. Ye, Y. Kong, C. Zhang, Y. Lv, S. Cheng, D. Hou and Y. Xian, *ACS Nano*, 2021, **15**, 14253–14262.

37 H. Li, X. Zhou, D. Yao and H. Liang, *Chem. Commun.*, 2018, **54**, 3520.

38 J.-X. Fan, D.-W. Zheng, W.-W. Mei, S. Chen, S.-Y. Chen, S.-X. Cheng and X.-Z. Zhang, *Small*, 2017, **13**, 1702714.